Chemical Engineering Journal 433 (2022) 133512

Contents lists available at ScienceDirect

Chemical Engineering Journal

journal homepage: www.elsevier.com/locate/cej

Hydroxyapatite-based biphasic catalysts with plasticity properties and its potential in carbon dioxide fixation

Jordi Sans [a,b,*], Marc Arnau [a,b], Vanesa Sanz [c], Pau Turon [c,*], Carlos Alemán [a,b,d,*]

[a] Departament d'Enginyeria Química, EEBE, Universitat Politècnica de Catalunya, C/ Eduard Maristany, 10-14, Ed. I2, 08019 Barcelona, Spain
[b] Barcelona Research Center in Multiscale Science and Engineering, Universitat Politècnica de Catalunya, C/ Eduard Maristany, 10-14, 08019 Barcelona, Spain
[c] B. Braun Surgical, S.A.U. Carretera de Terrasa 121, 08191 Rubí (Barcelona), Spain
[d] Institute for Bioengineering of Catalonia (IBEC), The Barcelona Institute of Science and Technology, Baldiri Reixac 10-12, 08028 Barcelona, Spain

ARTICLE INFO

Keywords:
Calcium phosphate
CO_2 reduction
Ethanol production
Heterogeneous catalysis
Polarized hydroxyapatite

ABSTRACT

The design of catalysts with controlled selectivity at will, also known as catalytic plasticity, is a very attractive approach for the recycling of carbon dioxide (CO_2). In this work, we study how catalytically active hydroxyapatite (HAp) and brushite (Bru) interact synergistically, allowing the production of formic acid or acetic acid depending on the HAp/Bru ratio in the catalyst. Raman, wide angle X-ray scattering, X-ray photoelectron spectroscopy, scanning electron microscopy and electrochemical impedance spectroscopy studies, combined with an exhaustive revision of the crystalline structure of the catalyst at the atomic level, allowed to discern how the Bru phase can be generated and stabilized at high temperatures. Results clearly indicate that the presence of OH^- groups to maintain the crystalline structural integrity in conjunction with Ca^{2+} ions less bonded to the lattice fixate carbon into C1, C2 and C3 molecules from CO_2 and allow the evolution from formic to acetic acid and acetone. In this way, the plasticity of the HAp-Bru system is demonstrated, representing a promising green alternative to the conventional metal-based electrocatalysts used for CO_2 fixation. Thus, the fact that no electric voltage is necessary for the CO_2 reduction has a very favorable impact in the final energetic net balance of the carbon fixation reaction.

1. Introduction

Conversion of carbon dioxide (CO_2) into high valuable chemical products is currently being extensively explored. Moreover, the use of CO_2 as feedstock for synthesizing commodity chemicals is an advantageous strategy considering both environmental and economic aspects [1–6]. However, obtaining profitable products is challenging due to the significant energetic cost of changing the oxidation state of carbon from + 4 in CO_2 to + 2 for carbon monoxide (CO) and formic acid/formiate (HCOOH / $HCOO^-$), to –2 for methanol (CH_3OH) or to –4 for methane (CH_4), which can be used as raw materials for industrial processes or as sustainable source of energy fuels [7]. For this reason, the use of metal–organic catalysts has been widely investigated [8,9], showing remarkable selectivity towards specific chemical species attributed to the capacity of generating $HCOO^-$ (Sn and Pb) [10–12] or to bind relevant intermediates, •COOH (Au, Ag, Pd, Zn, Bi) [13–17] and •CO (Cu) [18,19]. On the other hand, other alternatives are being explored as those catalysts have some disadvantages, such as low reduction activity, toxic effects on health and complicate synthesis processes, leading to high economic cost and a significant environmental impact [20]. Within this context, the concept catalytic plasticity is drawing increasing attention, as stands for controlling the selectivity of a catalyst by design through modifying its chemical composition, tuning its catalytic properties by treating them under specific conditions or controlling the reaction parameters. Although this is a quite novel paradigm with few publications reported, Rosenthal and co-workers [21] recently described the CO_2 reduction using bismuth with flexible catalytic properties, capable of generating $HCOO^-$ or CO depending on the ionic liquid used as a promoter.

Other alternatives have been studied to overcome the metal–organic hurdles and concerns, such as the use of inorganic compounds, carbon based materials, or heterogeneous metal electrocatalysts [18–24]. Recently, we reported a novel and highly promising catalyst based on polarized hydroxyapatite (HAp) capable of fixing CO_2 into high valuable chemical products, such as ethanol, methanol and formic acid, showing its high catalytic activity as the reactions were performed at mild

* Corresponding authors.
E-mail addresses: jordi.sans.mila@upc.edu (J. Sans), pau.turon@bbraun.com (P. Turon), carlos.aleman@upc.edu (C. Alemán).

https://doi.org/10.1016/j.cej.2021.133512
Received 19 September 2021; Received in revised form 31 October 2021; Accepted 3 November 2021
Available online 9 November 2021
1385-8947/© 2021 The Authors. Published by Elsevier B.V. This is an open access article under the CC BY-NC-ND license (http://creativecommons.org/licenses/by-nc-nd/4.0/).

conditions [25]. Due to its low-cost synthesis, abundancy and biocompatibility [26,27], HAp postulates as an excellent green catalyst with exceptional benefits from both economic and environmental perspective. To become catalytically active, HAp must undergo permanent structural changes where OH^- ions, organized in columns in the crystal lattice, are oriented in a specific direction via a thermal stimulation polarization (TSP) treatment [28,29]. TSP consists in exposing HAp to a strong electric voltage at high temperatures, which facilitates the generation of OH^- vacancies and the reorganization of OH^- columns that result in a permanent polarization and an enhancement of its electrical properties [30,31]. As a consequence, the catalytic activity of polarized HAp is governed by electron transport, availability of binding sites and affinity to adsorbate species of interest. Indeed, HAp catalytic activity might be tuned by following methods such as crystalline atomic modifications, creation of polymorphs, and combining the HAp with different electrocatalysts to generate synergistic effects, which have successfully been demonstrated for other catalytic systems [23,32,33].

In this work, we examine the plasticity properties of permanently polarized HAp by inducing the apparition of brushite (*i.e.* $CaHPO_4{\cdot}2H_2O$; Bru) through the synthesis and treatment, which is usually understood to be a precursor of more stable apatitic phases [34], at the surface of the catalyst. Thus, a new biphasic catalyst containing both HAp and Bru (hereafter named C-2) has been achieved by introducing small changes in the TSP process to enhance the exposition of the surface to a highly ionized atmosphere. The structure of the new C-2 catalyst has been completely characterized using Raman microscopy, wide angle X-ray scattering (WAXS), X-ray photoelectron spectroscopy (XPS), scanning electron microscopy (SEM) and electrochemical impedance spectroscopy (EIS). After this, the effect of the coexistent Bru phase in the selectivity and efficiency of carbon fixation reaction has been investigated and compared with the single-phase HAp catalyst (hereafter named C-1). The synergy observed between the HAp and Bru phases provides a promising avenue for developing HAp-based catalysts with controlled selectivity.

2. Experimental

2.1. Synthesis of hydroxyapatite catalytically active

The materials and the hydrothermal procedure used to prepare highly crystalline HAp powder are reported in the Supporting Information. After sintering for 2 h at 1000 °C, 150 mg of the obtained white HAp powder was pressed for 10 min at 620 MPa into disks of 5 mm of radius and ~ 1.5 mm of thickness. Catalytic activation was successfully achieved applying the TSP treatment, which consists in exposing the HAp disks at 500 V and 1000 °C for 1 h. After an exhaustive exploration of different conditions, these voltage, temperature and time of exposition values were found to be the optimum for delocalizing the charges through independent crystalline domains and for reinforcing the charge accumulation at the grain boundaries, maximizing the catalytic properties [30]. For obtaining single-phase HAp catalysts (C-1), the electrodes (two stainless steel AISI 304 plates) were placed in contact with the HAp disk. On the other hand, multiphasic HAp-Bru catalysts (C-2) were attained separating by 4 cm the positive electrode from the HAp disk, which was left in contact with the negative electrode. After several trials, this separation was found to be the optimal one to have a systematic and reproducible control in the formation of Bru on the surface of the disk.

2.2. Characterization of the catalyst

Structural and chemical characterization studies were conducted using scanning electron microscopy (SEM), X-ray photoelectron spectroscopy (XPS), micro-Raman spectroscopy, wide angle X-ray scattering (WAXS) and electrochemical impedance spectroscopy (EIS). From WAXS spectra, crystallinity (χ_c) and crystallite sizes L_{hkl} were determined. Description of the experimental details is provided in the Supporting Information.

2.3. Carbon fixation

Reactions were carried out in an inert reactor chamber loaded at room temperature with 3 bar CO_2 and 3 bar CH_4 and heated at 95 °C for 72 h under UV irradiation (GPH265T5L4, 253.7 nm). Before sealing, 0.5 mL of de-ionized liquid water were added to the reactor. It is worth noting that no electric field was applied during the catalytic process, the application of a voltage being only used for the preparation of the catalysts. The fact that polarized HAp is able to provide the suitable electrical conditions for the catalysis (*i.e.* without the use of external electrical field) drastically increases the final energetic net balance of the reaction. The products of the reaction, extracted from the catalyst surface, were analyzed by ^{1}H NMR spectroscopy (Bruker Avance III-400). Yields of the reaction were obtained by comparison with controlled concentration of the corresponding commercial products as a reference. Details are provided in the Supporting Information. Blank reactions were provided in previous work [25].

3. Results and discussion

3.1. Effect of TSP treatment on the coexistent brushite phase

Fig. 1a, which compares the WAXS spectra recorded for C-1 and C-2, reveals the unambiguous presence of highly crystalline HAp in both catalysts. Thus, the peaks identified at $2\theta = 31.8°$, $32.2°$, and $33.0°$ correspond to the (2 1 1), (1 1 2) and (3 0 0) reflections of HAp, respectively (JCPDS card number 9–0432). Moreover, the identification of the co-existent Bru in C-2 samples becomes difficult since most of its characteristic peaks overlap in position with other HAp reflections. The most significant peaks of Bru appear at $2\theta = 29°$, $31°$, $35°$, $42°$, and $51°$, which have been attributed to the (1 4 1), (2 2 $\bar{1}$), (1 2 1), (1 5 $\bar{2}$) and (1 4 $\bar{3}$) reflections, respectively (JCPDS card number 72–0713). As it can be seen, although the (2 2 $\bar{1}$), $2\theta = 31.0°$, is the only distinguishable reflection for Bru in Fig. 1a, comparison of the relative intensities obtained for C-1 and C-2 supports the presence of such co-existing calcium phosphate phases in the latter. One of the most relevant differences is observed at $2\theta = 51.3°$, which can be attributed to the (4 1 0) reflection of HAp or to the (1 4 $\bar{3}$) of Bru. For C-1 the intensity of the peak at $2\theta = 51.3°$ relative to the one at $2\theta = 52.1°$, which corresponds to the (4 0 2) HAp reflection, is lower than one ($I_{2\theta=51.0} / I_{2\theta=52.1} = 0.96$), indicating that the intensity of the former peak is slightly lower than that of the latter. For C-2, $I_{2\theta=51.0} / I_{2\theta=52.1}$ increases to 1.14, evidencing that the peak at $2\theta = 51.3°$ becomes more intense than the one at $2\theta = 52.1°$.

The (1 1 2) and (3 0 0) peaks were also used to determine the crystallinity (χ_c; Eq S1), whereas the (2 1 1) reflection was used to calculate the crystallite size (L_{211}; Eq S2). The crystallinity is very high and similar for the two catalysts, $\chi_c = 0.95 \pm 0.03$ and 0.92 ± 0.03 for C-1 and C-2, respectively. Crystallite sizes are also comparable for the two catalysts, the obtained values ($L_{211} = 75.2 \pm 2.4$ and 82.7 ± 3.72 nm for C-1 and C-2, respectively), being in agreement with those reported in the literature [35]. Overall, these observations indicate that the differences applied during the TSP treatment do not affect the predominant HAp phase.

We have recently reported the use of Raman microscopy as an alternative technique to obtain unequivocal determination of calcium phosphate phases [35]. Raman studies on C-1 and C-2 catalysts are presented in Fig. 1b. The spectra of calcium phosphate phases are mainly dominated by their characteristic P–O vibrations. The four characteristic regions of HAp, which correspond to the PO_4^{3-} internal modes, can be seen in the spectra of the catalysts, being: $\nu_1 = 962$ cm^{-1}, $\nu_2 = 390$–480 cm^{-1}, $\nu_3 = 570$–625 cm^{-1} and $\nu_4 = 1020$–1095 cm^{-1} [36,37]. Both samples present a slight splitting of the ν_1 mode in another two peaks at 970 and 949 cm^{-1}, which has been attributed to the different P–O

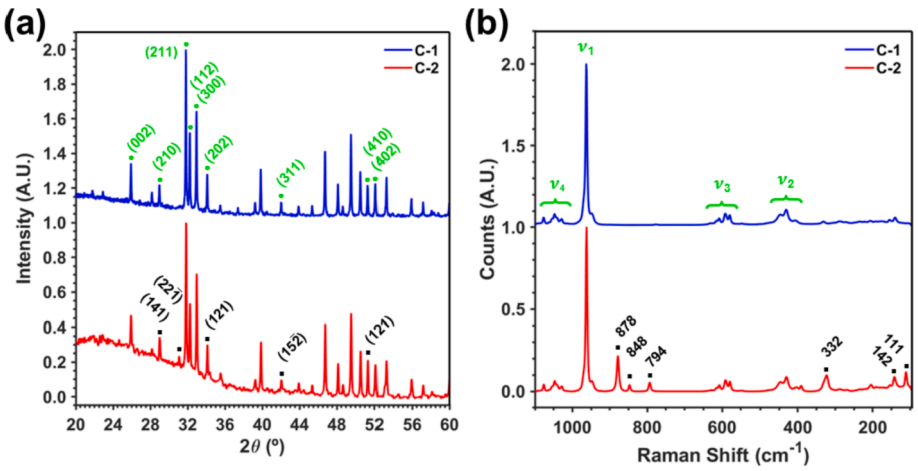

Fig. 1. (a) WAXS diffraction patterns in the characteristic 2θ range from 20° to 60° and (b) Raman spectra of the PO_4^{3-} internal modes (ν_1, ν_2, ν_3 and ν_4) for C-1 and C-2 catalysts. Characteristic reflections and vibrations for HAp and Bru are labelled in black and green, respectively.

stretching vibrations of the three crystallographic non-equivalent PO_4^{3-} tetrahedra found in the β-tricalcium phosphate (TCP) phase [38]. The presence of TCP is not related to the TSP treatment but to small variation in the conditions during the hydrothermal synthesis and the sintering applied afterwards [27]. Moreover, previous studies showed that the TSP treatment increases the crystallinity and reduces TCP phase by imposing crystallographic specific orientations [35]. Besides, the fact that the two samples present approximately the same relative amount of TCP (*i.e.* the ratio of the intensities of the shoulder at 970 cm^{-1} and the main peak at 962 cm^{-1}, $I_{970/962}$, is 0.12 and 0.10 for C-1 and C-2 respectively) evidences that differences in the conditions applied during the TSP treatment are not the trigger of the TCP generation. However, the effect of separating the positive electrode from the mineral disc during the TSP treatment is clearly manifested in Fig. 1b.

The evident presence of HPO_4^{2-} and POH vibrations allows tracking the variations in the amount of Bru, depending on the TSP conditions. In this sense, the synergistic activity between the HAp and Bru phases is strongly dependent on their exposed surfaces and, therefore, the

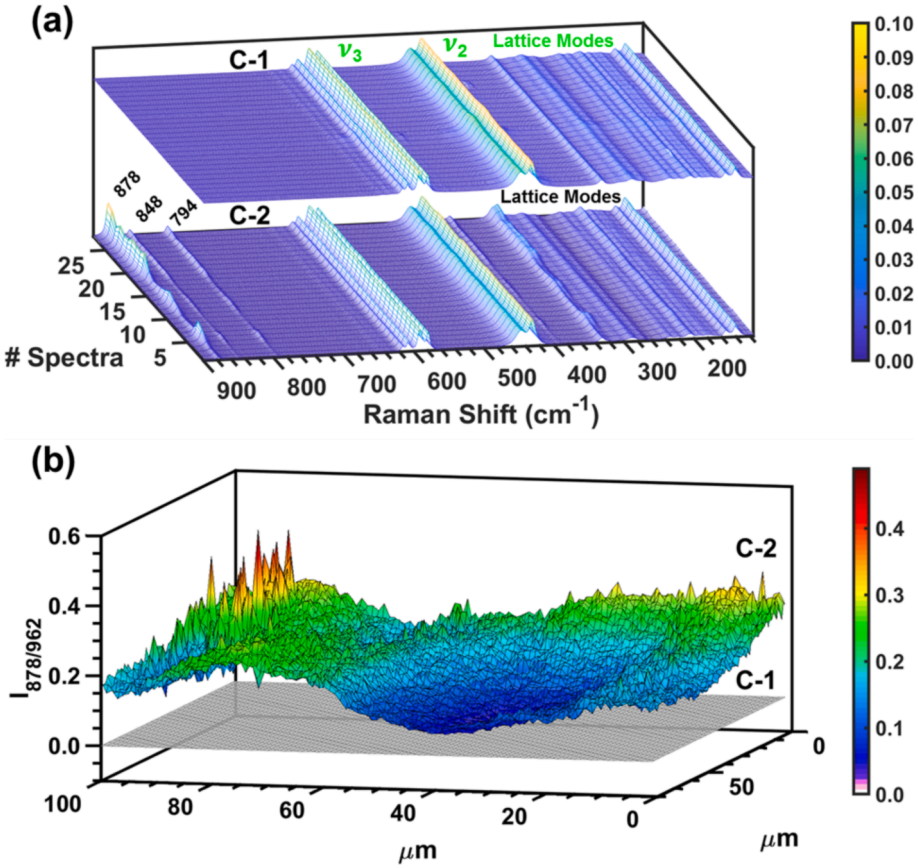

Fig. 2. For the C-1 and C-2 catalysts: (a) Stacked Raman spectra obtained from a 7 × 4 array with a spacing of 1 μm for the C-1 and C-2 catalysts. Scale bar refers to the relative intensity of the peaks; (b) Raman maps tracking the Bru / HAp composition through the ratio between the intensities of their principal peaks at 878 and 962 cm^{-1} ($I_{878/962}$). Maps consist on 8000 points spectra acquisition with a 1 μm spacing.

characterization of their superficial distribution is of major interest. Fig. 2a depicts 28 Raman spectra of C-1 and C-2 samples, which have recorded from a 7 × 4 array with a spacing of 1 μm. For clarity purposes, all spectra have been stacked together, the scale bar referring to the relative intensity of the peaks. As expected, the C-1 spectra do not show any trace of the Bru peaks aforementioned, in comparison with C-2 sample. Surprisingly, the 878 cm^{-1} peak of C-2, which corresponds to the HPO_4^{2-} normal vibration mode, varies in its relative intensity up to 90%, indicating that the coexisting Bru phase is distributed very heterogeneously. Characterization of the Bru / HAp ratio by considering the ratio between the intensities of their principal peaks at 879 and 962 cm^{-1} ($I_{878/962}$), which is presented in Fig. 2b, confirms that Bru forms an extremely heterogeneous interface for C-2 sample (*i.e.* the average value is $I_{878/962}$ is 0.17 with refined overall relative variation of ~ 95%) while C-1 remains pure HAp for larger areas. On the other hand, in-depth Raman studies showed that Bru generation is a superficial phenomenon, as is discussed in the Electronic Supporting Information (Figure S1). Results derived from Fig. 2 suggest that the geometry of the set-up used to apply the electric field plays an important role, defining the heterogeneity of the two co-existing phases.

In order to support this conclusion, we conducted additional experiments repeating the TSP treatment under controlled modifications of

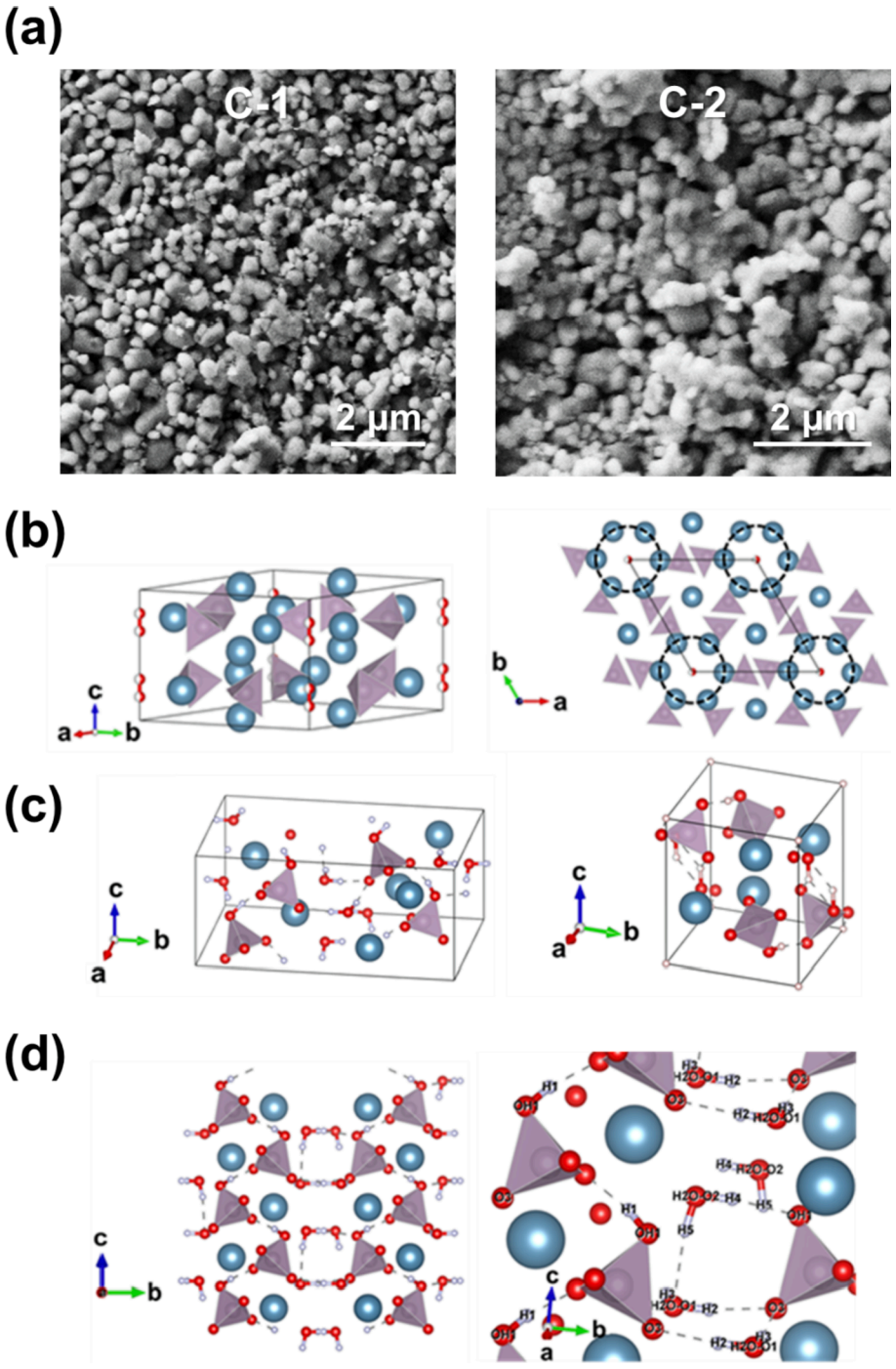

Fig. 3. (a) SEM micrograph of C-1 and C-2 catalysts. Schemes displaying: (b) the HAp crystalline structure: Unitary cell (left) and apical perspective of OH^- channels (circled) along the c axis (right); (c) the unit cell of Bru (left) and monetite (right); and (d) the crystalline structure of Bru. The atoms involved in the hydrogen bonds have been labeled.

distance and geometry between positive and negative electrodes. More specifically, in a specific assay to assess the geometry of the electrode, the cylindrical plate was removed, leaving only the cooper wire acting as positive electrode. Examination of the recorded Raman spectra (Figure S2) confirmed the dependence of the Bru phase with the geometry of the applied electric field (Figure S2). Not only the peaks HPO_4^{2-} and POH vibration peaks appeared to be more intense (*i.e.* $I_{878/962} = 0.73$ and $I_{794/962} = 0.17$ for the C-2 catalysts prepared without and with plate at the positive electrode, respectively), but noteworthy the sample resulted to be more homogenous after treatment, the peak at 878 cm^{-1} showing a relative variation of ~ 21 % only. Overall, results demonstrate that the Bru / HAp ratio and heterogeneity of the catalyst can be controlled by varying the distance between the plates and modifying the geometry of the electric field during the TSP treatment. In spite of differences in the composition and distribution of calcium phosphate phases, SEM micrographs revealed that the size and morphology of C-1 and C-2 catalyst microstructure do not exhibit significant differences (Fig. 3a). Both consisted on agglomerates of up to 1 μm formed by 100 to 300 nm nanoparticles.

In summary, the co-existence of Bru and HAp in C-2 was demonstrated by WAXS through the apparition of the (22 $\bar{1}$) reflection at $2\theta = 31.0°$ and the relative intensities of the reflections at $2\theta = 51.3°$ and 52.1°. This was confirmed by Raman spectroscopy that allowed us to identify the peaks associated to the normal vibration mode of HPO_4^{2-}, the POH deformation mode and the POH rotation mode. However, the distribution of Bru phase among the predominant HAp phase was only disclosed by Raman maps recorded at different depths. The recorded spectra evidenced that, although HAp is still the predominant phase, Bru is heterogeneously distributed at the surface of the C-2 catalyst, changing the uniform interfacial microstructure of C-1.

3.2. Structural characterization of the C-2 catalyst

In order to understand the synergistic effects occurring in Bru-containing catalyst, exhaustive structural characterization is deemed to be crucial. In the case worked, our efforts have been focused on discerning how Bru was integrated into the HAp crystal lattice as distortion on its boundaries, generating new active edge sites and modifying locally the electric properties.

The most common polymorph of HAp is the hexagonal lattice (Fig. 3b) belonging to the space group $P6_3/m$ (a = b = 9.432 Å, c = 6.881 Å; $\alpha = \beta = 90°$, $\gamma = 120°$) [39]. PO_4^{3-} groups are ordered in equivalent tetrahedra while Ca^{2+} ions occupy two different crystallographic positions. In this crystalline structure, the OH^- groups are aligned in columns along the *c*-axis but with disordered orientations because of electrostatic forces. Upon application of the TSP treatment, remaining OH^- groups tend to orient themselves along the specific direction of the electric field, thus introducing crystallographic stress in the crystal lattice facilitated by the creation of vacancies during TSP treatment. Such crystallographic stress is shown for C-1 in Fig. 4a, which displays a magnification of the Raman spectrum in the region of the $\nu 1$ principal mode. Whereas the main ν_1 vibration mode of HAp in C-2 sample coincides with its theoretical value at 962 cm^{-1}, C-1 main peak is located at 963 cm^{-1}, reflecting the tensile strain of the PO_4^{3-} tetrahedra. The fact that C-1 is the only sample presenting such shift indicates that Bru found in the C-2 catalyst compensates the local tensile stress tension induced by re-arrangement of the OH^- chains.

One of the most surprising aspects of the C-2 catalyst is that the attainment of the Bru phase is apparently contradictory with the fact that the TSP is carried out at high temperatures. At around 160 °C, Bru starts dehydrating to monetite ($CaHPO_4$) for further deprotonation to the γ, β and α different forms of calcium pyrophosphate ($Ca_2P_2O_7$) when the temperature increases to 320, 700 and 1200 °C, respectively [40,41]. The experimental evidence obtained from the HPO_4^{2-} and the POH vibration modes at 878, 848 and 794 cm^{-1}, as well as the absence of the POP vibration at around 732 cm^{-1}, allows to discard the presence of $Ca_2P_2O_7$. The discrimination of Bru from monetite is clearly visualized by analyzing the lattice vibration modes since such structures crystallize in different space groups, as reflected in Fig. 3c. Bru consists on a monoclinic structure with an *Ia* space group symmetry (a = 5.799 Å, b = 15.126 Å, c = 6.184 Å; $\alpha = \gamma = 90°$, $\beta = 116.428°$) [42], while monetite exhibits a triclinic unit cell with a $P\bar{1}$ space group symmetry (a = 6.916 Å, b = 6.619 Å, c = 6.946 Å; $\alpha = 96.180°$, $\beta = 103.82°$, $\gamma = 88.34°$) [43]. The lattice modes of the C-1 and C-2 catalysts are compared in Fig. 4b. C-1 presents the characteristic lattice modes of HAp at: 140 and 155 cm^{-1} (attributed to the transitional vibrations of $Ca_1 + Ca_2$ and Ca_2, respectively); 193 and 205 cm^{-1} (translational vibration of PO_4^{3-}); 235 and 288 cm^{-1} (librational vibrations of PO_4^{3-}); 270 cm^{-1} (transitional vibration of Ca_1); and 332 cm^{-1} (translational vibrations of OH^-) [36].

In comparison with C-1, the spectrum recorded for C-2 displays much more intense peaks at 111, 142 and 270 cm^{-1}, which have been attributed to the contribution of the Ca^{2+} unique crystallographic sites in Bru [33,39]. Moreover, the PO_4^{3-} translational mode at 205 cm^{-1} is enhanced in C-2 with respect to C-1. Is it worth noting that, while the peak at 142 cm^{-1} (assigned to the transitional vibrations of $Ca_1 + Ca_2$ of HAp and Ca of Bru) is much more intense and presents a red shift of 2 cm^{-1} with respect to C-1, the peak at 155 cm^{-1} remains unaltered, as it has been attributed to the HAp transitional vibration of Ca_2, which is inexistent in the Bru phase. The red shift of Ca^{2+} transitional vibration from 140 cm^{-1} in C-1 to 142 cm^{-1} in C-2 confirms the presence of Bru in the latter, instead of monetite. Thus, due to group symmetries, the Raman shift attributed to the Ca^{2+} transitional vibration should be ordered as follows: monetite < HAp < Bru. Overall, results shown in Fig. 4a-b not only confirms the presence of Bru but also highlights that the C-2 catalyst locally presents Ca^{2+} with higher mobility and less tensile stress, which could cause a synergistic effect responsible of an enhancement of its catalytic performance.

The presence of Bru instead of monetite opens the door to a new topic regarding the structural integrity of the former in the C-2 catalyst. As shown in Fig. 3d, the crystal structure of Bru can be understood as a layered system formed by zig-zag Ca^{2+} and PO_4^{3-} alternated chains

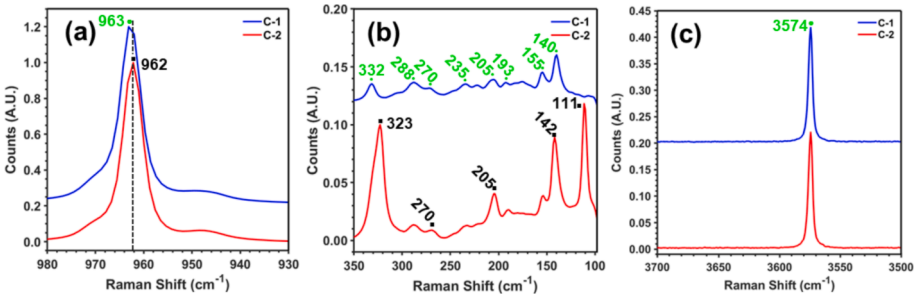

Fig. 4. In-depth analyses of Raman spectra of C-1 and C-2 of the zones of interest: (a) $\nu 1$ principal mode; (b) lattice modes; and (c) O–H stretching vibrational mode in the region of 3500 to 3700 cm^{-1}. Characteristic Raman vibrations for HAp and Bru are labelled in black and green, respectively.

parallel to the *a*-axis and growing along the *c*-axis. These chains are bonded together along the *b*-axis through hydrogen bonds, provided by H_2O molecules which form an intermediate layer. However, this water intermediate layer has not been detected in the Raman spectrum of C-2. Characteristic stretching modes for water should be detected as two duplets at 3539 and 3483 cm^{-1} for ν_1, and 3270 and 3163 cm^{-1} for ν_2. Fig. 4c shows the characteristic HAp peak corresponding to the OH^- stretching mode of HAp at 3574 cm^{-1}. Moreover, neither the water librational modes, which are typically located at 678 cm^{-1}, can be appreciated in Fig. 1b.

Detailed analysis of the lattice modes displayed in Fig. 4b revealed the presence of a strong new peak at 323 cm^{-1} for C-2, which has been assigned to the translational vibration modes of OH^- groups. This peak can be clearly deconvoluted into two different peaks located at 332 cm^{-1}, which matches the translational vibration of HAp obtained in the C-1 spectrum, and at 323 cm^{-1} (Figure S3). The fact that this new peak presents an important blue shift indicates the existence of a different crystallographic OH^- with less mobility, and thus, somehow bonded. Due to their participation in hydrogen bonding interaction, H_2O molecules of pure Bru are distorted from that of free molecules, generating two distinct crystallographic sites for water molecules (labeled in Fig. 3d as H2O-O1 and H2O-O2). The external layers are bonded together via the O3···H2 (of H2O-O1) and OH1···H4 (of H2O-O2) hydrogen bond interactions, presenting short distances of 1.81 Å and 1.90 Å and almost linear angles of 167.3° and 175.7° respectively [41,42]. Taking into account the theoretical aspects aforementioned and in agreement with the experimental results obtained, we propose that hydroxyl groups occupying the crystallographic positions of water molecules are responsible of stabilizing the crystallographic Bru-like phase though hydrogen bonding interactions. The exchange of proton and hydroxyl groups at high temperatures, causing modifications in the crystalline structure of HAp, has been widely studied [35,44]. However, substituting H_2O molecules by OH^- may cause other crystallographic distortions since the remaining water proton, which is hydrogen bonded to other oxygen of the lattice, is suppressed. For the case of H2O-O2 water molecule this is not crucial for the stability of Bru, as H5 is weakly bonded to the H2O-O1 water molecule, with a H5···H2O-O1 distance of 2.16 Å. Accordingly, the alternating Ca^{2+} and PO_4^{3-} ions form weaker interactions, and thus have more mobility. This hypothesis is supported by the drastic increment in the intensity of the lattice modes for such ions in the C-2 catalyst (Fig. 4b).

On the other hand, H2O-O1 water molecule is also hydrogen bonded to the O3 of a PO_4^{3-} group, with a distance of 1.78 Å. In this case, to determine which hydrogen bond is substituted by the OH^- is harder, as they are energetically very similar. However, hypothesizing a combination of OH^- ions pointing in both directions (O3···H2 and H3···O3) might be reasonable since the TSP treatment imposes a specific OH^- orientation, whereas OH1···H4 and O3···H2 are pointing backwards.

Similar OH^- rearrangements have been reported before, when studying the electrical activation of HAp through proton hopping along the *c*-axis among electroactive O^{2-} anions [45]. Such new configurations should be expected to present low stability since they could be either expelled (if close to the surface) or reabsorbed in the HAp lattice. In order to corroborate such hypothesis, C-2 long term structural stability studies were considered. C-2 remained mostly unaltered for 60 days, showing a measurable 44% decrease of the Bru ratio after 120 days. This observation suggested a semi-permanent Brushite conformation, which is in agreement with the aforementioned study [45]. Nevertheless, TSP treatment was applied again afterwards, recovering the Bru phase and without showing any kind of structural fatigue. This feature is proved in Fig. 5a, which compares the Raman spectra in the region of 750 to 1200 cm^{-1} for the same C-2 catalyst as prepared, after 120 days, and repolarized by applying the TSP treatment after 120 days. All in all, the structural stability and the reversible customization of C-1 ↔ C-2 catalysts have been stressed out.

In order to quantify the enhancement in the lattice mobility of Ca^{2+} ions highlighted by Raman spectroscopy, XPS measurements were conducted to capture the surface electron binding states of Ca. Fig. 5b compares the XPS Ca 2p of C-1 and C-2 catalysts. Both spectra present the characteristic Ca $2p_{3/2}$ and Ca $2p_{1/2}$ peaks of HAp located at 346.9 and 350.5 eV for C-1 and 346.4 and 350.0 eV for C-2. This observation is in good agreement with recent XPS studies on HAp after TSP treatment [30,31].

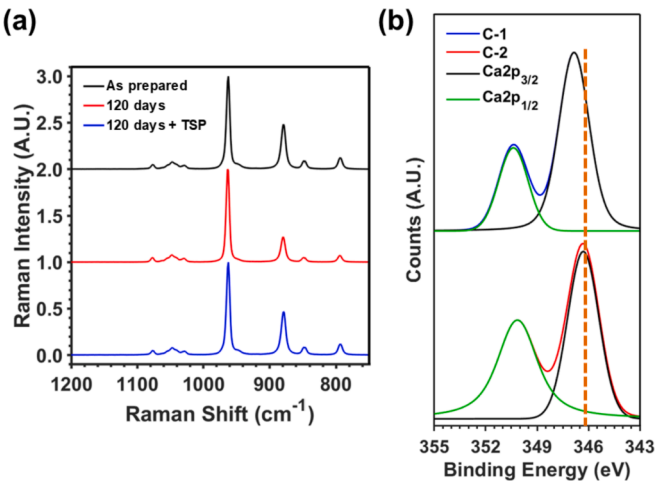

Fig. 5. (a) Raman spectra of C-2 in the region of 750 to 1200 cm^{-1} as prepared, after 120 days and repolarized by applying the TSP treatment after 120 days. (b) XPS spectra of Ca 2p obtained for C-1 and C-2 catalysts.

The binding energy of the Ca 2p peak is mainly related with the Ca···PO_4^{3-} bonds. The standard value of Ca $2p_{3/2}$ is usually measured at ~ 347.2 eV, even though shifts at higher binding energies are observed in some cases, for example when $RCOO^-$ groups are adsorbed (*i.e.* Ca···COO^- bonds are stronger than Ca···PO_4^{3-} bonds) [46]. Conversely, shifts to smaller binding energies are appreciated for C-1 and C-2, which has been associated to the OH^- vacancies generated by the TSP treatment. In agreement with the Raman spectra, the shift is more pronounced for the C-2 sample (–0.8 eV) than for the C-1 sample (–0.3 eV). This 0.5 eV difference has been attributed to the presence of the Bru coexistent phase in the C-2 catalyst.

3.3. *Effect of the brushite presence on the catalyst selectivity*

The exhaustive analysis accomplished in previous sections allowed elucidating the structural differences between the C-1 and C-2 catalysts, highlighting some possible synergies between the two phases detected in the latter. More specifically, the effects of the coexisting Bru phase on the catalytic properties of HAp can be anticipated as follows: 1) Ca^{2+} ions have smaller binding energy and, thus, can act as new catalytic or adsorption sites; and 2) even though the presence of OH^- is maintained in both phases, the symmetry of ordered OH^- columns may be broken in the boundaries between phases, creating regions with lower electron conductivity but with higher accumulated charge. EIS measurements were carried out to confirm the latter hypothesis (Fig. 6 and Table S1). The electrical equivalent circuit (EEC) derived from the fitting of the experimental data showed that the capacitance at the surface of the C-2 catalyst is twice that of C-1. More specifically, the constant phase element (CPE), which represents a real capacitor with current leakage in the EEC, is 55.94 and 103.76 $\mu F \cdot (cm^2 \cdot s^{n-1})^{-1}$ for C-1 and C-2, respectively. Additional details are provided in the Electronic Supporting Information.

In order to ascertain the possible contributing synergies by the Bru phase, carbon fixation reactions have been conducted using the C-1 and C-2 catalysts for comparison. More specifically, reactions have been catalyzed in an inert reaction chamber (120 mL) using a CO_2 and CH_4 starting gas mixture (3 bar each) and liquid water (1 mL) under

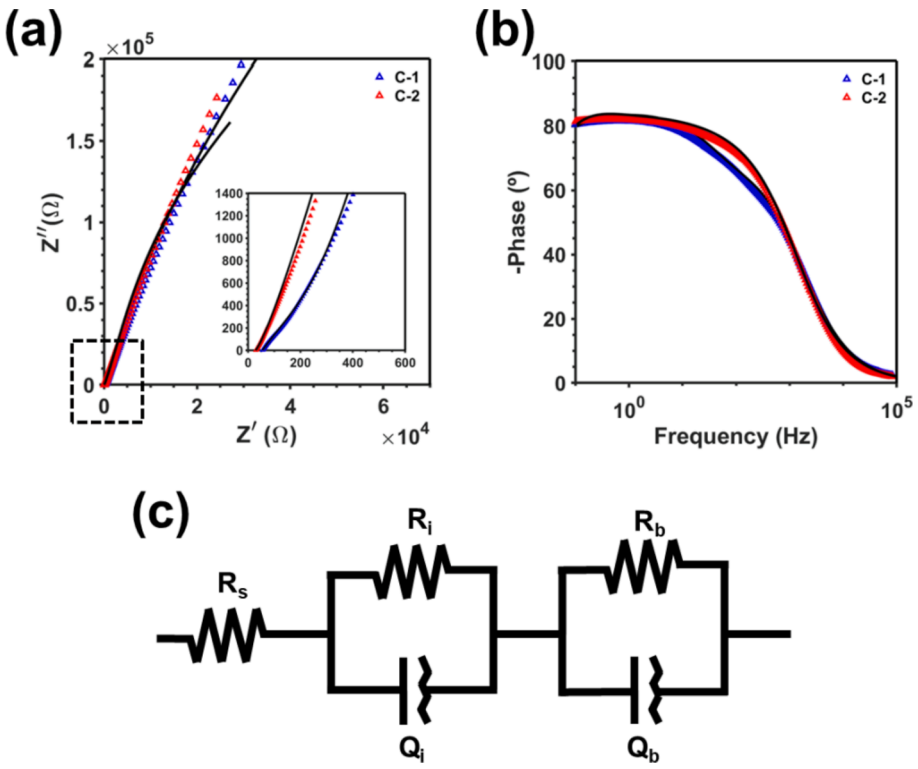

Fig. 6. (a) Nyquist and (b) Bode plots obtained for C-1 and C-2 catalysts. (c) EEC modeled considering the existence of both HAp bulk and an HAp/Bru interface (noted as "b" and "i", respectively) as shown by the Raman maps and in-depth studies. R_s corresponds to the electrolyte resistance. Experimental data (blue and red for C-1 and C-1, respectively) fit perfectly with the EEC (black lines). All the circuit elements are listed in Table S1 and present low error percentages, stressing out the reliability of the models used.

irradiation of an UV lamp illuminating directly the catalysts at 95 °C. It is worth noting that the utilization of a CO_2 and CH_4 gas mixture as feeding results in the formation of a variety of compounds [25], which is richer than that obtained when CO_2 is used alone [47]. Therefore, in order to prove the plasticity of the catalyst, the CO_2 and CH_4 mixture has been considered more suitable than CO_2 alone as reaction medium. It should be mentioned that, in previous work, we proved that non-polarized HAp does not catalyze the carbon fixation reaction that converts CO_2 and CH_4 into ethanol [25]. The reactor, which is sketched in Fig. 7, was equipped with inlet valves for CH_4 and CO_2 feeding and an outlet valve to recover the gaseous reaction products. An UV lamp (GPH265T5L/4, 253.7 nm) was also placed in the middle of the reactor to irradiate the catalyst directly, the lamp being protected by a UV transparent quartz tube. All surfaces were coated with a thin film of a perfluorinated polymer. Accordingly, the reaction medium was in contact with the catalyst surface but not with the reactor surfaces, which allowed us to discard other catalyst effects.

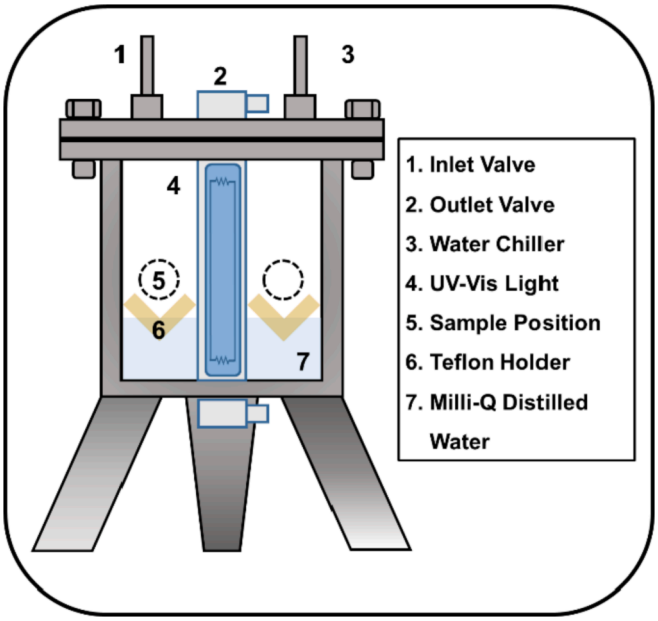

Fig. 7. Details of the reactor designed for the carbon fixation reaction.

Fig. 8 presents the ^{1}H NMR spectra obtained after 72 h reaction from the C-1 and C-2 catalysts dissolved in deuterated water containing 100 mM HCl and 50 mM NaCl, which allowed us to identify the reaction products formed on the surface of the catalysts. Three reaction products were clearly identified for both catalysts by inspecting the spectra at the low frequency region (Fig. 8a): ethanol (CH_2 quartet the CH_3 triplet at 3.50 and 1.06 ppm, respectively), acetone (CH_3 singlet at 2.08 ppm), and acetic acid (CH_3 singlet at 1.85 ppm). The OH peak of ethanol, which is the predominant product in both cases (*i.e.* 13.13 ± 3.75 and 15.01 ± 4.62 μmol per gram of catalyst for C-1 and C-2, respectively), overlaps with the intense water peak at 4.65 ppm (not shown). In any case, the two spectra displayed in Fig. 8a are qualitatively similar, indicating that the coexistence of Bru does not play any significant effect on the yield of ethanol, but it significantly increases the yield of acetone and acetic acid.

In contrast, analysis of the spectra ^{1}H NMR at the high frequency region (Fig. 8b) reveals a very important and noticeable difference. More specifically, formic acid (singlet at 8.28 ppm) and a peak at 5.81 ppm, which has been attributed to traces of double bonded carbon atoms are detected for C-1 sample only. This is an important achievement since the yield of formic acid, 8.06 ± 1.89 μmol, from C-1 is very high, reaching 36% of the total yields (*vs.* 59% for ethanol). Table 1 summarizes the yields of the reactions using C-1 and C-2.

It is worth noting that the ethanol yields listed in Table 1 are comparable to those reported for different carbon fixation reactions, as for example, the hydrogenation of CO_2 to ethanol using Zr_{12}-bpdc-$Cu^{II}Li$ and CuI@Zr_{12}-bpdc catalyst [48] and the direct synthesis of ethanol from CO_2 and H_2 using titania supported gold nanoclusters as catalyst [49]. However, those reactions required less practical conditions (*i.e.* higher pressures and temperatures) [48,49]. Similarly, the thermal

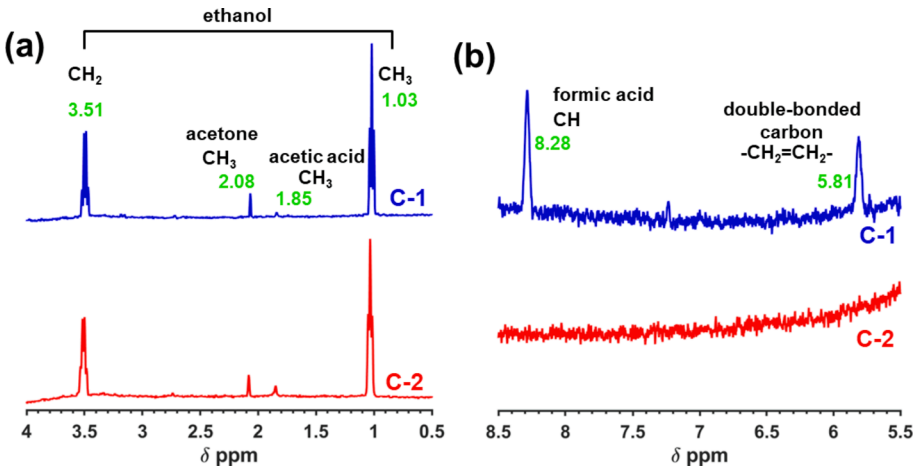

Fig. 8. ^{1}H NMR spectra of the regions at: (a) 0.5 to 4.0 ppm, (b) 5.5 to 8.5 ppm.

Table 1
Yields (in μmol of product per gram of catalyst) for all the products of the reactions catalyzed by C-1 and C-2.

Catalyst	Acetone	Acetic Acid	Ethanol	Formic Acid
C-1	0.9 ± 0.24	0.26 ± 0.05	13.13 ± 3.75	8.06 ± 1.89
C-2	1.31 ± 0.29	0.65 ± 0.13	15.01 ± 4.62	0

reduction of CO_2 to carbon products using perovskite-type titanium nanocatalysts requires temperatures higher than 400 °C [50]. CO_2 has been also photo-converted in different organic products, such as cyclohexanone and cyclohexyl formate, using UV radiation and $ZnFe_2O_4$/TiO_2 as photocatalysts [51]. Interestingly, UV irradiation is not necessary to activate the conversion of CO_2 in valuable organic products when C-1 and C-2 are the catalysts. Another relevant feature is that we obtained a low fraction of acetic acid, which was also achieved converting a mixture of CO_2 and CH_4 on a zinc modified zeolite but at a temperature range of 250–500 °C [52]. Thus, the reaction conditions used in the processes catalyzed by C-1 and C-2 are, in general, milder than those reported for other reactions involving the catalytic transformation of CO_2 in other valuable chemicals.

A possible mechanism for the formation of ethanol is displayed in Scheme 1. In this mechanism, the binding mode of the likely intermediate, *CO, to the catalyst is through the carbon. After reduction, the ethanol synthesis is obtained by reaction with $^{\bullet}CH_3$ from methane.

To further understand the selectivity differences between C-1 and C-2 catalysts, yields of the reaction with respect to ethanol production (Fig. 9a) and C-2/C-1 product ratios (Fig. 9b) have been analyzed. In order to compare different products, the areas of ^{1}H NMR spectra were properly normalized as described in the Supporting Information (Eq. S3-S6). Firstly, the total catalytic activity ratio, which is defined by the C-2_{total}/C-1_{total} ratio (where C-2_{total} and C-1_{total} refers to all the products obtained using the C-2 and C-1 catalysts, respectively), is higher than 0.9. The fact that this value is close to 1 indicates that tuning the catalyst by introducing a new phase does not have any important effect in the total catalytic activity but only in the selectivity. Thus, the acetone, acetic acid and ethanol yields are higher for C-2 than for C-1, compensating the amount of formic acid generated. Furthermore, results evidence that the coexistence of the HAp and Bru phases facilitates the incorporation of $\bullet CH_3$, favoring the conversion of formic acid to acetic acid. Consistently, the yield of acetone is higher for C-2 than for C-1. It is worth mentioning that when the Bru phase predominates over the HAp phase, as for example for the sample prepared without plate at the positive electrode (Figure S2), the catalytic activity is lost (not shown).

Overall, incorporation of small amounts of Bru phase in polarized HAp-based catalysts enhances the incorporation of $\bullet CH_3$ species in CO_2 and CH_4 fixation reactions. This has been attributed to: 1) charge accumulation that favors the dissociation of CH_4 to $\bullet CH_3$; and 2) Ca^{2+} ions are more susceptible to adsorb species as they are less bonded. These results are potentially interesting for other carboxylation reactions that can be carried out under mild conditions.

4. Conclusions

The generation of Bru at high temperatures in the HAp crystal lattice creates regions with different proton conductivity and adsorption capacity in the HAp catalyst structure, which are responsible for the catalytic synergies between the two calcium phosphate phases. In this sense, the catalytic selectivity in the CO_2 and CH_4 fixation reaction, which occurs under mild conditions, can be controlled using single-phase (C-1) or biphasic (C-2) catalysts. HAp-based catalysts with a small amount of Bru can be easily achieved during the TSP treatment by modifying the distance between plates used as electrodes. Moreover, the drastic variation of the electrode geometry and orientation of the electric field results in an excessive amount of Bru that hinders the catalytic activity.

In summary, this study demonstrates that the introduction of modifications in the crystal structure of HAp-based catalysts by incorporating other calcium phosphate phases, such as Bru, creates synergistic effects that affect the selectivity and increases the efficiency of the remaining catalyzed reaction products. These results open new avenues to a promising family of HAp-based green catalysts with catalytic plasticity properties that increment the added value of a sustainable carbon fixation. Thus, an important advantage of HAp-based catalysts with respect to conventional electrocatalysts is that the CO_2 reduction occurs without

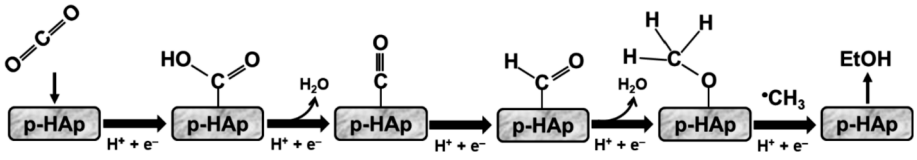

Scheme 1. Mechanism proposed for the formation of ethanol.

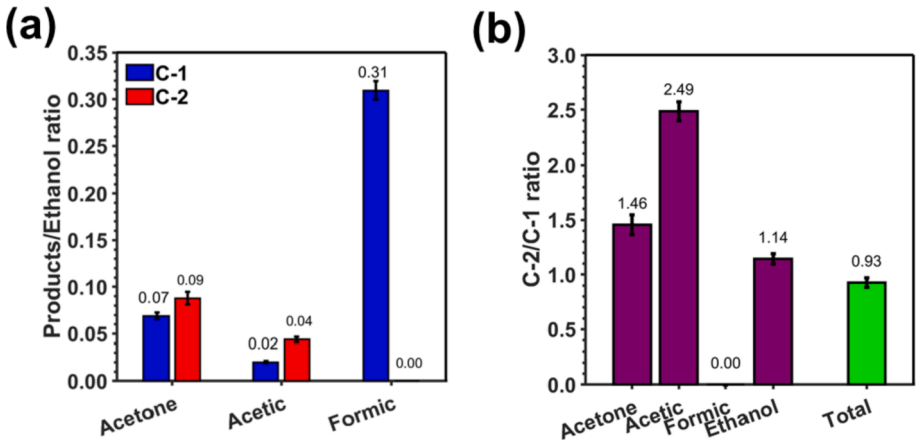

Fig. 9. Comparison of catalytic performance of C-1 and C-2 catalysts: (a) ratio of products/ethanol, (b) C-2/C-1 ratio of all the products detected.

applying an electric field, which drastically increases the final energetic net balance of the carbon fixation process.

Declaration of Competing Interest

The authors declare that they have no known competing financial interests or personal relationships that could have appeared to influence the work reported in this paper.

Acknowledgement

Authors acknowledge MINECO-FEDER (RTI2018-098951-B-I00), Agència de Gestió d'Ajuts Universitaris i de Recerca (2017SGR359) and B. Braun Surgical, S.A.U and B. Braun Melsungen AG for financial support. Special thanks to Dr. Meinrad Lugan, Dr. Hans-Otto Maier and Dr. Sonja Rauschwalbe for their support to the OLi project.

References

[1] F. Li, A. Thevenon, A. Rosas-Hernández, Z. Wang, Y. Li, C.M. Gabardo, A. Ozden, C. T. Dinh, J. Li, Y. Wang, J.P. Edwards, Y.i. Xu, C. McCallum, L. Tao, Z.-Q. Liang, M. Luo, X. Wang, H. Li, C.P. O'Brien, C.-S. Tan, D.-H. Nam, R. Quintero-Bermudez, T.-T. Zhuang, Y.C. Li, Z. Han, R.D. Britt, D. Sinton, T. Agapie, J.C. Peters, E. H. Sargent, Molecular tuning of CO_2-to-ethylene conversion, Nature. 577 (7791) (2020) 509–513, https://doi.org/10.1038/s41586-019-1782-2.

[2] R. Sharifian, R.M. Wagterveld, I.A. Digdaya, C. Xiang, D.A. Vermaas, Electrochemical carbon dioxide capture to close the carbon cycle, Energy Environ. Sci. 14 (2) (2021) 781–814, https://doi.org/10.1039/D0EE03382K.

[3] S.-L. Hou, J. Dong, B. Zhao, Formation of C-X bonds in CO_2 chemical fixation catalyzed by metal−organic frameworks, Adv. Mater. 32 (3) (2020) 1806163, https://doi.org/10.1002/adma.v32.310.1002/adma.201806163.

[4] Y. Wu, Z. Jiang, X.u. Lu, Y. Liang, H. Wang, Domino electroreduction of CO_2 to methanol on a molecular catalyst, Nature 575 (7784) (2019) 639–642, https://doi.org/10.1038/s41586-019-1760-8.

[5] J. Gao, H. Zhang, X. Guo, J. Luo, S.M. Zakeeruddin, D. Ren, M. Grätzel, Selective C-C coupling in carbon dioxide electroreduction via efficient spillover of intermediates as supported by operando raman spectroscopy, J. Am. Chem. Soc. 141 (47) (2019) 18704–18714, https://doi.org/10.1021/jacs.9b0741510.1021/jacs.9b07415.s001.

[6] W. Zhang, Y.i. Hu, L. Ma, G. Zhu, Y. Wang, X. Xue, R. Chen, S. Yang, Z. Jin, Progress and perspective of electrocatalytic CO_2 reduction for renewable carbonaceous fuels and chemicals, Adv. Sci. 5 (1) (2018) 1700275, https://doi.org/10.1002/advs.201700275.

[7] M. Aresta, A. Dibenedetto, A. Angelini, From CO_2 to chemicals, materials, and fuels: the role of catalysis, in: Encycl. Inorg. Bioinorg. Chem., John Wiley & Sons, Ltd, Chichester, UK, 2014 pp. 1–18. https://doi.org/10.1002/9781119951438.eibc2257.

[8] P.P. Power, Main-group elements as transition metals, Nature 463 (7278) (2010) 171–177, https://doi.org/10.1038/nature08634.

[9] L. Fan, C. Xia, F. Yang, J. Wang, H. Wang, Y. Lu, Strategies in catalysts and electrolyzer design for electrochemical CO_2 reduction toward C2+ products, Sci. Adv. 6 (2020) eaay3111, https://doi.org/10.1126/sciadv.aay3111.

[10] H. Li, C. Oloman, Development of a continuous reactor for the electro-reduction of carbon dioxide to formate – Part 1: Process variables, J. Appl. Electrochem. 36 (10) (2006) 1105–1115, https://doi.org/10.1007/s10800-006-9194-z.

[11] A. Del Castillo, M. Alvarez-Guerra, J. Solla-Gullón, A. Sáez, V. Montiel, A. Irabien, Electrocatalytic reduction of CO_2 to formate using particulate Sn electrodes: Effect of metal loading and particle size, Appl. Energy. 157 (2015) 165–173, https://doi.org/10.1016/j.apenergy.2015.08.012.

[12] Q. Zhu, J. Ma, X. Kang, X. Sun, H. Liu, J. Hu, Z. Liu, B. Han, Efficient reduction of CO_2 into formic acid on a lead or tin electrode using an ionic liquid catholyte mixture, Angew. Chemie Int. Ed. 55 (31) (2016) 9012–9016, https://doi.org/10.1002/anie.201601974.

[13] D.D. Zhu, J.L. Liu, S.Z. Qiao, Recent advances in inorganic heterogeneous electrocatalysts for reduction of carbon dioxide, Adv. Mater. 28 (18) (2016) 3423–3452, https://doi.org/10.1002/adma.v28.1810.1002/adma.201504766.

[14] D.R. Kauffman, D. Alfonso, C. Matranga, H. Qian, R. Jin, Experimental and computational investigation of Au25 clusters and CO2: A unique interaction and enhanced electrocatalytic activity, J. Am. Chem. Soc. 134 (2012) 10237–10243, https://doi.org/10.1021/ja303259q.

[15] L. Zhang, Z. Wang, N. Mehio, X. Jin, S. Dai, Thickness- and particle-size-dependent electrochemical reduction of carbon dioxide on thin-layer porous silver electrodes, ChemSusChem. 9 (5) (2016) 428–432, https://doi.org/10.1002/cssc.201501637.

[16] D. Gao, H.u. Zhou, J. Wang, S. Miao, F. Yang, G. Wang, J. Wang, X. Bao, Size-dependent electrocatalytic reduction of CO_2 over Pd nanoparticles, J. Am. Chem. Soc. 137 (13) (2015) 4288–4291, https://doi.org/10.1021/jacs.5b00046.

[17] J. Rosen, G.S. Hutchings, Q.i. Lu, S. Rivera, Y. Zhou, D.G. Vlachos, F. Jiao, Mechanistic insights into the electrochemical reduction of co$_2$ to co on nanostructured Ag surfaces, ACS Catal. 5 (7) (2015) 4293–4299, https://doi.org/10.1021/acscatal.5b00840.

[18] J.H. Montoya, C. Shi, K. Chan, J.K. Nørskov, Theoretical insights into a co dimerization mechanism in CO_2 electroreduction, J. Phys. Chem. Lett. 6 (11) (2015) 2032–2037, https://doi.org/10.1021/acs.jpclett.5b00722.

[19] H. Mistry, A.S. Varela, C.S. Bonifacio, I. Zegkinoglou, I. Sinev, Y.-W. Choi, K. Kisslinger, E.A. Stach, J.C. Yang, P. Strasser, B.R. Cuenya, Highly selective plasma-activated copper catalysts for carbon dioxide reduction to ethylene, Nat. Commun. 7 (2016) 12123, https://doi.org/10.1038/ncomms12123.

[20] J. Schneider, H. Jia, J.T. Muckerman, E. Fujita, Thermodynamics and kinetics of CO_2, CO, and H^+ binding to the metal centre of CO_2 reduction catalysts, Chem. Soc. Rev. 41 (6) (2012) 2036–2051, https://doi.org/10.1039/C1CS15278E.

[21] A. Atifi, D.W. Boyce, J.L. DiMeglio, J. Rosenthal, Directing the outcome of CO_2 reduction at bismuth cathodes using varied ionic liquid promoters, ACS Catal. 8 (4) (2018) 2857–2863, https://doi.org/10.1021/acscatal.7b0343310.1021/acscatal.7b03433.s001.

[22] Q. Zhu, J. Ma, X. Kang, X. Sun, J. Hu, G. Yang, B. Han, Electrochemical reduction of CO_2 to CO using graphene oxide/carbon nanotube electrode in ionic liquid/acetonitrile system, Sci. China Chem. 59 (5) (2016) 551–556, https://doi.org/10.1007/s11426-016-5584-1.

[23] M.S. Faber, S. Jin, Earth-abundant inorganic electrocatalysts and their nanostructures for energy conversion applications, Energy Environ. Sci. 7 (11) (2014) 3519–3542, https://doi.org/10.1039/C4EE01760A.

[24] M. Zeng, Y. Li, Recent advances in heterogeneous electrocatalysts for the hydrogen evolution reaction, J. Mater. Chem. A. 3 (29) (2015) 14942–14962, https://doi.org/10.1039/C5TA02974K.

[25] J. Sans, G. Revilla-López, V. Sanz, J. Puiggalí, P. Turon, C. Alemán, Permanently polarized hydroxyapatite for selective electrothermal catalytic conversion of carbon dioxide into ethanol, Chem. Commun. 57 (42) (2021) 5163–5166, https://doi.org/10.1039/D0CC07989H.

[26] A. Szcześ, L. Hołysz, E. Chibowski, Synthesis of hydroxyapatite for biomedical applications, Adv. Colloid Interface Sci. 249 (2017) 321–330, https://doi.org/10.1016/j.cis.2017.04.007.

[27] A. Haider, S. Haider, S.S. Han, I.-K. Kang, Recent advances in the synthesis, functionalization and biomedical applications of hydroxyapatite: a review, RSC Adv. 7 (13) (2017) 7442–7458, https://doi.org/10.1039/C6RA26124H.

[28] M. Rivas, L.J. del Valle, P. Turon, C. Alemán, J. Puiggalí, Sustainable synthesis of amino acids by catalytic fixation of molecular dinitrogen and carbon dioxide, Green Chem. 20 (3) (2018) 685–693, https://doi.org/10.1039/C7GC02911J.

[29] G. Revilla-López, J. Sans, J. Casanovas, O. Bertran, J. Puiggalí, P. Turon, C. Alemán, Analysis of nitrogen fixation by a catalyst capable of transforming N_2, CO_2 and CH_4 into amino acids under mild reactions conditions, Appl. Catal. A Gen. 596 (2020) 117526, https://doi.org/10.1016/j.apcata.2020.117526.
[30] J. Sans, M. Arnau, F. Estrany, P. Turon, C. Alemán, Regulating the superficial vacancies and OH^- orientations on polarized hydroxyapatite electrocatalysts, Adv. Mater. Interfaces. 8 (11) (2021) 2100163, https://doi.org/10.1002/admi.v8.1110.1002/admi.202100163.
[31] M. Rivas, L.J. delValle, E. Armelin, O. Bertran, P. Turon, J. Puiggalí, C. Alemán, Hydroxyapatite with permanent electrical polarization: preparation, characterization, and response against inorganic adsorbates, ChemPhysChem. 19 (14) (2018) 1746–1755, https://doi.org/10.1002/cphc.v19.1410.1002/cphc.201800196.
[32] M.A. Lukowski, A.S. Daniel, C.R. English, F. Meng, A. Forticaux, R.J. Hamers, S. Jin, Highly active hydrogen evolution catalysis from metallic WS2 nanosheets, Energy Environ. Sci. 7 (8) (2014) 2608–2613, https://doi.org/10.1039/C4EE01329H.
[33] J. Greeley, J.K. Nørskov, L.A. Kibler, A.M. El-Aziz, D.M. Kolb, Hydrogen evolution over bimetallic systems: understanding the trends, ChemPhysChem. 7 (5) (2006) 1032–1035, https://doi.org/10.1002/(ISSN)1439-764110.1002/cphc.v7:510.1002/cphc.200500663.
[34] R.L. Frost, Y. Xi, R.E. Pogson, G.J. Millar, K. Tan, S.J. Palmer, Raman spectroscopy of synthetic $CaHPO_4{\cdot}2H_2O$- and in comparison with the cave mineral brushite, J. Raman Spectrosc. 43 (4) (2012) 571–576, https://doi.org/10.1002/jrs.v43.410.1002/jrs.3063.
[35] J. Sans, J. Llorca, V. Sanz, J. Puiggalí, P. Turon, C. Alemán, Electrically polarized hydroxyapatite: influence of the polarization process on the microstructure and properties, Langmuir 35 (46) (2019) 14782–14790, https://doi.org/10.1021/acs.langmuir.9b0252210.1021/acs.langmuir.9b02522.s001.
[36] Z. Iqbal, V.P. Tomaselli, O. Fahrenfeld, K.D. Möller, F.A. Ruszala, E. Kostiner, Polarized Raman scattering and low frequency infrared study of hydroxyapatite, J. Phys. Chem. Solids. 38 (8) (1977) 923–927, https://doi.org/10.1016/0022-3697(77)90132-9.
[37] S. Koutsopoulos, Synthesis and characterization of hydroxyapatite crystals: A review study on the analytical methods, J. Biomed. Mater. Res. 62 (4) (2002) 600–612, https://doi.org/10.1002/(ISSN)1097-463610.1002/jbm.v62:410.1002/jbm.10280.
[38] P.N. de Aza, F. Guitián, C. Santos, S. de Aza, R. Cuscó, L. Artús, Vibrational properties of calcium phosphate compounds. 2. comparison between hydroxyapatite and β-tricalcium phosphate, Chem. Mater. 9 (4) (1997) 916–922, https://doi.org/10.1021/cm9604266.
[39] G. Ma, X.Y. Liu, Hydroxyapatite: Hexagonal or monoclinic? Cryst. Growth Des. 9 (7) (2009) 2991–2994, https://doi.org/10.1021/cg900156w.
[40] A. Dosen, R.F. Giese, Thermal decomposition of brushite, CaHPO4·2H2O to monetite $CaHPO_4$ and the formation of an amorphous phase, Am. Mineral. 96 (2011) 368–373, https://doi.org/10.2138/am.2011.3544.
[41] P.F. Schofield, K.S. Knight, J.A.M.V.D. Houwen, E. Valsami-Jones, The role of hydrogen bonding in the thermal expansion and dehydration of brushite, di-calcium phosphate dihydrate, Phys. Chem. Miner. 31 (9) (2004) 606–624, https://doi.org/10.1007/s00269-004-0419-6.
[42] C.I. Sainz-Díaz, A. Villacampa, F. Otálora, Crystallographic properties of the calcium phosphate mineral, brushite, by means of First Principles calculations, Am. Mineral. 89 (2-3) (2004) 307–313, https://doi.org/10.2138/am-2004-2-308.
[43] M. Catti, G. Ferraris, A. Filhol, Hydrogen bonding in the crystalline state. $CaHPO_4$ (monetite), P1 or P1? A novel neutron diffraction study, Acta Crystallogr. Sect. B Struct. Crystallogr. Cryst. Chem. 33 (1977) 1223–1229, https://doi.org/10.1107/S0567740877005706.
[44] K. Yamashita, K. Kitagaki, T. Umegaki, Thermal instability and proton conductivity of ceramic hydroxyapatite at high temperatures, J. Am. Ceram. Soc. 78 (1995) 1191–1197, https://doi.org/10.1111/j.1151-2916.1995.tb08468.x.
[45] A. Laghzizil, N. Elherch, A. Bouhaouss, G. Lorente, T. Coradin, J. Livage, Electrical behavior of hydroxyapatites $M_{10}(PO_4)_6(OH)_2$ (M = Ca, Pb, Ba), Mater. Res. Bull. 36 (2001) 953–962.
[46] M.C. Chang, J. Tanaka, XPS study for the microstructure development of hydroxyapatite–collagen nanocomposites cross-linked using glutaraldehyde, Biomaterials 23 (18) (2002) 3879–3885, https://doi.org/10.1016/S0142-9612(02)00133-3.
[47] J. Sans, V. Sanz, P. Turon, C. Alemán, Enhanced CO_2 conversion into ethanol by permanently polarized hydroxyapatite through C−C coupling. ChemCatChem (2021) in press. https://doi.org/10.1002/cctc.202101157.
[48] B. An, Z. Li, Y. Song, J. Zhang, L. Zeng, C. Wang, W. Lin, Cooperative copper centres in a metal–organic framework for selective conversion of CO_2 to ethanol, Nat. Catal. 2 (8) (2019) 709–717, https://doi.org/10.1038/s41929-019-0308-5.
[49] D. Wang, Q. Bi, G. Yin, W. Zhao, F. Huang, X. Xie, M. Jiang, Direct synthesis of ethanol via CO_2 hydrogenation using supported gold catalysts, Chem. Commun. 52 (99) (2016) 14226–14229, https://doi.org/10.1039/C6CC08161D.
[50] T. Watanabe, T. Ohba, Low-temperature CO_2 thermal reduction to graphitic and diamond-like carbons using perovskite-type titanium nanoceramics by quasi-high-pressure reactions, ACS Sustainable Chem. Eng. 9 (10) (2021) 3860–3873, https://doi.org/10.1021/acssuschemeng.0c0896310.1021/acssuschemeng.0c08963.s001.
[51] G. Song, F. Xin, X. Yin, Photocatalytic reduction of carbon dioxide over $ZnFe_2O_4$/TiO_2 nanobelts heterostructure in cyclohexanol, J. Colloid Interface Sci. 442 (2015) 60–66, https://doi.org/10.1016/j.jcis.2014.11.039.
[52] J.-F. Wu, S.-M. Yu, W.D. Wang, Y.-X. Fan, S. Bai, C.-W. Zhang, Q. Gao, J. Huang, W. Wang, Mechanistic insight into the formation of acetic acid from the direct conversion of methane and carbon dioxide on zinc-modified h–zsm-5 zeolite, J. Am. Chem. Soc. 135 (36) (2013) 13567–13573, https://doi.org/10.1021/ja406978q.